

Lattice distortion leads to glassy thermal transport in crystalline $\text{Cs}_3\text{Bi}_2\text{I}_6\text{Cl}_3$

Ze Zhu Zeng,^{1,*} Zheyong Fan,² Michele Simoncelli,^{3,4} Chen Chen,^{5,†}
Ting Liang,⁶ Yue Chen,⁷ Geoff Thornton,⁸ and Bingqing Cheng^{9,1,‡}

¹The Institute of Science and Technology Austria, Am Campus 1, 3400 Klosterneuburg, Austria

²College of Physical Science and Technology, Bohai University, Jinzhou 121013, China

³Theory of Condensed Matter Group of the Cavendish Laboratory, University of Cambridge, United Kingdom

⁴Department of Applied Physics and Applied Mathematics, Columbia University, New York (USA)

⁵School of Physical Sciences, Great Bay University, Dongguan, Guangdong, China

⁶Department of Electronic Engineering and Materials Science and Technology Research Center, The Chinese University of Hong Kong

⁷Department of Mechanical Engineering, The University of Hong Kong, Pokfulam Road, Hong Kong SAR, China

⁸London Centre for Nanotechnology, University College London, London WC1H 0AJ, United Kingdom

⁹Department of Chemistry, University of California, Berkeley, CA, USA

(Dated: December 23, 2024)

The glassy thermal conductivities observed in crystalline inorganic perovskites such as $\text{Cs}_3\text{Bi}_2\text{I}_6\text{Cl}_3$ is perplexing and lacking theoretical explanations. Here, we first experimentally measure such its thermal transport behavior from 20 K to 300 K, after synthesizing $\text{Cs}_3\text{Bi}_2\text{I}_6\text{Cl}_3$ single crystals. Using path-integral molecular dynamics simulations driven by machine learning potentials, we reveal that $\text{Cs}_3\text{Bi}_2\text{I}_6\text{Cl}_3$ has large lattice distortions at low temperatures, which may be related to the large atomic size mismatch. Employing the Wigner formulation of thermal transport, we reproduce the experimental thermal conductivities based on lattice-distorted structures. This study thus provides a framework for predicting and understanding glassy thermal transport in materials with strong lattice disorder.

A foundational theory for the lattice thermal conductivity (κ) in crystals was proposed by Peierls in 1929 [1] based on the phonon gas picture: κ has a T^3 behavior at low temperatures, followed by a decrease with a T^{-1} dependence due to Umklapp phonon scattering. This behavior is observed in many materials, such as thermoelectric AgTeI_2 [2] and inorganic perovskite CsPbI_3 [3], as illustrated in Fig. 1.

For glasses, such as SiO_2 [4] and B_2O_3 [5], the behavior of κ is distinct (see Fig. 1): At low temperatures ($T \lesssim 1$ K), $\kappa(T) \sim T^2$, which may be explained by quantum tunneling [6]; between 5 K and 25 K, $\kappa(T)$ plateaus, which may be related to the boson peak of glasses [7]; At higher T , κ increases with temperature, which can be explained by the Allen-Feldman (AF) model [8, 9] based on couplings between quasi-degenerate atomic vibrational modes.

However, κ of some crystalline materials do not follow the typical behavior of crystals but are rather glassy, e.g. layered perovskite $\text{Cs}_3\text{Bi}_2\text{I}_6\text{Cl}_3$ [10], quasi-one-dimensional perovskite BaTiS_3 [11, 12], and Ruddlesden-Popper perovskites $\text{Ba}_3\text{Zr}_2\text{S}_7$ and $\text{Ba}_4\text{Zr}_2\text{S}_{10}$ [13]. In this study, we synthesized a high-quality single crystal (see Methods section for details) of $\text{Cs}_3\text{Bi}_2\text{I}_6\text{Cl}_3$ (space group $P\bar{3}m1$) and measured its κ from 20 K to 300 K (see Fig. 1). Interestingly, both κ_x and κ_z in $\text{Cs}_3\text{Bi}_2\text{I}_6\text{Cl}_3$ deviate from the expected T^3 dependence at low T and lack crystalline-like peak in the entire temperature range. In addition, κ_x exhibits an unusual wide plateau region (60–150 K), while κ_z steadily increases with increasing temperature.

Some other materials also exhibit measured glassy κ below room temperature. For example, $(\text{KBr})_{1-x}(\text{KCN})_x$ [14, 15]

transitions from crystalline to glassy κ with an increase in the molar fraction of KCN, which was attributed to binary doping. The glassy κ in clathrates $\text{Sr}_8\text{Ga}_{16}\text{Ge}_{30}$ and $\text{Eu}_8\text{Ga}_{16}\text{Ge}_{30}$ [16] was rationalized by the rattling atoms within cage-like structures. In contrast, $\text{Cs}_3\text{Bi}_2\text{I}_6\text{Cl}_3$ lacks the binary doping as mixed crystals or a cage-like structure, suggesting a distinct mechanism behind its glassy κ . Acharyya *et al.* [10] first reported the glassy κ of crystalline $\text{Cs}_3\text{Bi}_2\text{I}_6\text{Cl}_3$, and rationalized the slow increase of κ near room temperature based on local atomic disorder and low sound velocity, but the mechanism governing the glassy κ at lower temperatures remains unclear.

It is challenging to calculate κ for solids with strong anharmonicity at low temperatures: Regular molecular dynamics (MD) does not consider nuclear quantum effects (NQE). Quantum MD methods, such as path integral MD (PIMD) [18], centroid MD (CMD) [19], ring polymer MD (RPMD) [20], and thermostatted ring polymer MD (TRPMD) [21], can incorporate the quantum delocalization of nuclei and quantum thermodynamic properties, while they cannot address real-time dynamic properties and thus require approximations for the non-linear heat flux operator [22, 23]. There is still debate on whether these quantum MD methods are accurate for computing thermal conductivities: Luo *et al.* [22] reported that RPMD combined with the Green-Kubo theory could reproduce the κ of ice Ih from 150 K to 200 K. Moreover, they argued that there is no essential difference between CMD and RPMD in computing quantum thermal conductivity, while TRPMD slightly underestimates κ of ice. However, Manolopoulos *et al.* [23] observed significant overestimation of Green-Kubo κ using CMD for liquid para-hydrogen below 30 K. They attributed these errors to the classical heat capacities used in CMD and proposed a quantum heat capacity scaling to achieve better agreement with experiments.

On the other hand, recent advancements [24] in lattice dynamics such as Wigner transport equation (WTE) [24–26] and

* zzen@ist.ac.at

† ccmln@gbu.edu.cn

‡ bingqingcheng@berkeley.edu

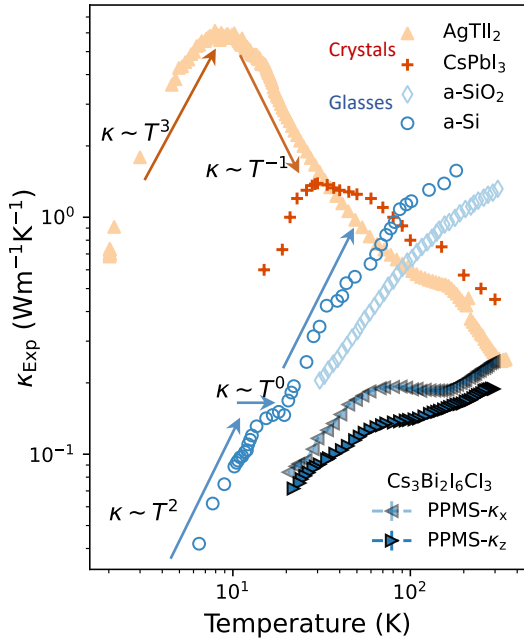


FIG. 1. Experimental lattice thermal conductivity (κ) for AgTlI_2 [2] and CsPbI_3 [3] crystals, amorphous Si [17] and SiO_2 [4] glasses, and single crystal $\text{Cs}_3\text{Bi}_2\text{I}_6\text{Cl}_3$ measured by us for both parallel (κ_z) and perpendicular ($\kappa_x = \kappa_y$) directions relative to the Bridgman growth direction.

quasi harmonic Green-Kubo (QHGK) theory [27, 28], by accounting for both (intra-band) propagation (κ_P) and (inter-band, Zener-like tunneling) coherence (κ_C) thermal conductivities, offer new methods to compute κ of complex materials accounting for the Bose-Einstein statistics of vibrations, anharmonicity and disorder. For crystals, both WTE and QHGK can accurately compute the bulk limit of κ by integrating microscopic, mode-resolved vibrational properties over the entire Brillouin zone (BZ), and example applications include WTE for perovskite CsPbBr_3 [25] and QHGK for diamond-cubic silicon [29]. For glasses, calculating the bulk limit of the conductivity requires ensuring that the finite-size atomistic models are large enough to realistically describe amorphicity. Various methods have been developed to address this challenge [30–33]. These methods share the key feature that when glassy atomistic models are sufficiently large to capture disorder, the conductivity remains unchanged upon further increasing the model size or applying different boundary conditions at the simulation-domain boundaries [34]. In practice, to verify this, one must check that the conductivity remains unchanged when predicted using increasingly larger cells with standard periodic boundary conditions (PBC); an additional test is to verify that the PBC κ is equivalent to κ computed by averaging over many different boundary conditions [31, 33]. The former test practically corresponds to performing calculations at $\mathbf{q} = \mathbf{0}$ only in models with increasingly larger size, while the latter corresponds to finding unchanged κ when comparing a calculation at $\mathbf{q} = \mathbf{0}$ only with one performed by averaging over wavevectors $\mathbf{q} \neq \mathbf{0}$

belonging to the small BZ of the disordered model.

Lattice distortion at low temperatures

We first constructed a machine-learning-based neuroevolution potential (NEP) [36] version 4 [37], for $\text{Cs}_3\text{Bi}_2\text{I}_6\text{Cl}_3$ across a broad range of temperature and strain, based on the PBEsol functional [38] with the D3 dispersion correction [39]. We then simulated the crystal structure of $\text{Cs}_3\text{Bi}_2\text{I}_6\text{Cl}_3$ between 25 K and 300 K. A $5 \times 5 \times 10$ supercell with 3,500 atoms was used to perform NEP PIMD simulations. Fig. 2a shows the projection of atom positions onto the two-dimensional a - b plane in a single unit cell with 10-fold replication ($1 \times 1 \times 10$) along the z direction. At 250 K, all atoms vibrate near their equilibrium lattice positions in the $P\bar{3}m1$ crystal structure, consistent with results of the crystal structure characterization from our single-crystal XRD experiment at 300 K (Table S2 of Supplementary Information (SI)). In contrast, at 25 K the atomic position distributions have multiple peaks. At 100 K, the peaks grow in size but become closer together, suggesting a reduction in lattice distortion but with stronger thermal vibrations. To the best of our knowledge, this distortion and related disorder-to-order transition is reported for the first time in this work. This distortion also exhibits a special correlation. Specifically, we selected a neighboring cell adjacent to the reference cell (shown in Fig. 2a) and performed the same analysis of the atomic probability distribution along the a - b plane (see Fig. S4). The results reveal that the projection patterns of the two cells are remarkably similar. Moreover, the distortion pattern also depends on the supercell size used to capture the disorder. Using a larger supercell ($7 \times 7 \times 10$) for RPMD simulations at 25 K revealed a distinct distortion pattern (Fig. S5). Larger supercells accommodate more commensurate soft modes, enhancing disorder through collective coupling (as discussed later).

Note that the scattered spots at 25 K and 100 K still cluster around the $P\bar{3}m1$ lattice sites, thus the calculated radial distribution functions (RDF) in Fig. 2b based on RPMD simulations show characteristic peaks associated with crystals across the whole temperature range. We compared the RDF (see Fig. S6) at 25 K, 100 K, and 250 K computed from RPMD and classical MD simulations. The RDF at 25 K exhibits a distinct difference, with the RDF from the RPMD simulations showing a broader first peak. This result indicates that, despite all atoms in $\text{Cs}_3\text{Bi}_2\text{I}_6\text{Cl}_3$ being relatively heavy, PIMD-based simulations are necessary to accurately assess the structural and thermodynamic properties of the system.

To further quantify the lattice distortion, we computed the mean square displacement (MSD) of the four elements based on RPMD trajectories, using the $P\bar{3}m1$ structure as a reference. As shown in Fig. 2c, MSD decreases with increasing temperature, with a notable drop between 200 K and 250 K that corresponds to the structure transition from disorder to order. Above 250 K, as the crystal structure reverts to the $P\bar{3}m1$ phase, MSD values increase with temperature, which is a typical tendency in ordered crystals. We also compared the MSD obtained from RPMD and classical MD simulations (Fig. S7).

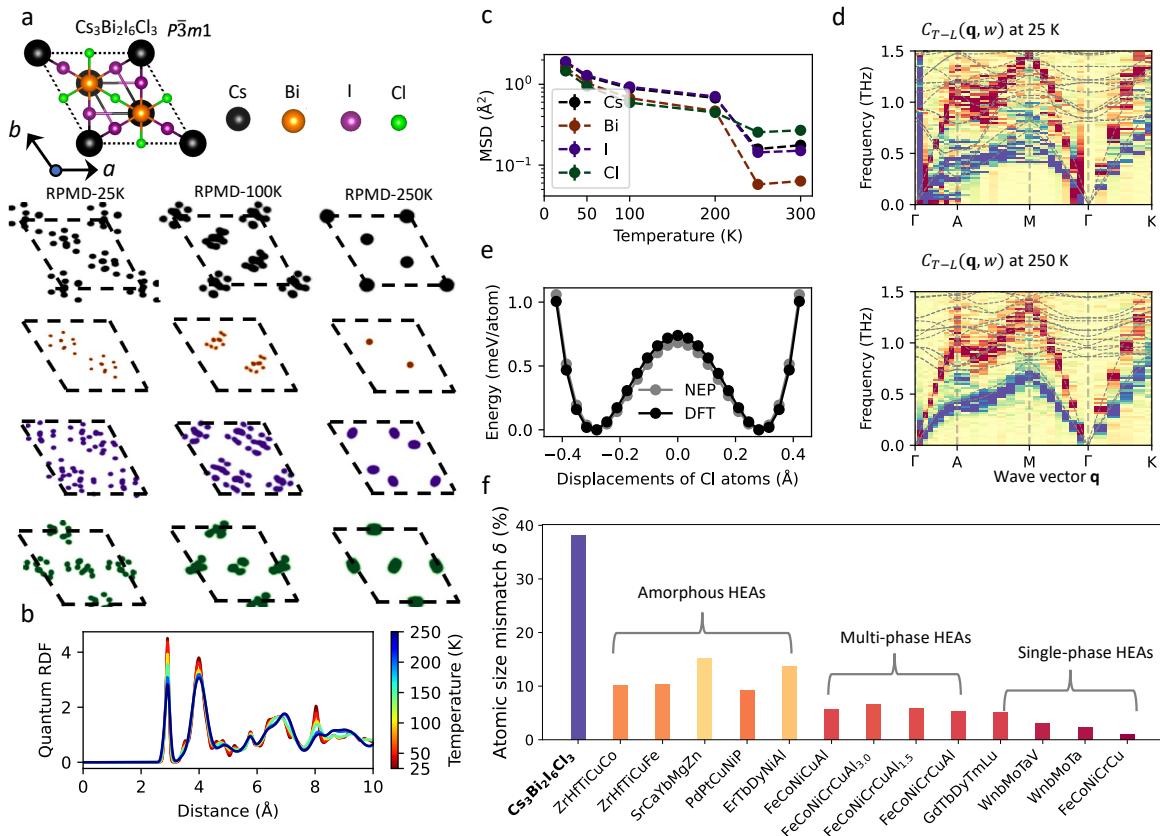


FIG. 2. **a** Atomic probability distribution of four elements in $\text{Cs}_3\text{Bi}_2\text{I}_6\text{Cl}_3$ from NEP ring-polymer molecular dynamics (RPMD) simulations with a $5 \times 5 \times 10$ supercell (3500 atoms) at 25 K, 100 K, and 250 K. **b** Calculated radial distribution function (RDF) of $\text{Cs}_3\text{Bi}_2\text{I}_6\text{Cl}_3$ at different temperatures based on the RPMD simulations with a 678-atoms supercell. **c** Mean square displacements (MSD) from 25 K to 300 K computed from NEP ring-polymer molecular dynamics (RPMD) simulations with a $5 \times 5 \times 10$ supercell (3500 atoms), using the $P\bar{3}m1$ crystalline $\text{Cs}_3\text{Bi}_2\text{I}_6\text{Cl}_3$ as the reference structure. **d** Transverse (red) and longitudinal (blue) current correlation functions $C_{T-L}(\mathbf{q}, \omega)$ as a function of wave vector \mathbf{q} and frequency ω , calculated from RPMD trajectories at 25 K and 250 K with a $16 \times 16 \times 16$ supercell (57344 atoms). The dashed curves show phonon dispersions of $\text{Cs}_3\text{Bi}_2\text{I}_6\text{Cl}_3$, computed using the temperature-dependent effective potential (TDEP) approach with the $P\bar{3}m1$ crystal structure. **e** Potential energy surfaces of the soft mode at Γ point calculated using NEP and DFT by displacing Cl atoms in the unit cell. **f** Atomic size mismatch parameter (δ) for crystalline $\text{Cs}_3\text{Bi}_2\text{I}_6\text{Cl}_3$ and selected high-entropy alloys (HEAs) [35] with single-phase, multiple-phase, and amorphous-phase structures.

The results highlight the importance of PIMD-based simulations in capturing accurate atomic vibrations at temperatures below 100 K, as the MSD from RPMD is significantly higher than that from classical MD at 25 K and 50 K.

The strong disorder in crystalline $\text{Cs}_3\text{Bi}_2\text{I}_6\text{Cl}_3$ at low temperatures is unusual for two reasons: First, in many disordered crystals, only a part of elements exhibit spatially correlated disorder [40, 41], where lattice distortions follow a specific pattern with spatial correlations, e.g. in thermoelectric PbTe the Pb atoms exhibit large deviation along specific $\langle 100 \rangle$ directions [42], in metal-organic frameworks [43] the correlated distribution of linker vacancies leads to a patterned disordering. In contrast, all elements in $\text{Cs}_3\text{Bi}_2\text{I}_6\text{Cl}_3$ have disorder. Second, the other disordered crystals are typically ordered at low T and become disordered at high T [40], while $\text{Cs}_3\text{Bi}_2\text{I}_6\text{Cl}_3$ is opposite.

Strong lattice distortion can lead to substantial phonon-

disorder scatterings. To investigate this, we used a $16 \times 16 \times 16$ supercell with 57344 atoms to compute the longitudinal and transverse current correlation functions based on RPMD trajectories at 25 K and 250 K (as shown in Fig. 2d with heatmaps), which incorporates both full-order lattice anharmonicity and NQE. The longitudinal and transverse current correlation functions [44], $C_L(\mathbf{q}, t)$ and $C_T(\mathbf{q}, t)$ are

$$\begin{aligned} C_L(\mathbf{q}, t) &= \frac{1}{N} \langle \mathbf{j}_L(\mathbf{q}, t) \cdot \mathbf{j}_L(-\mathbf{q}, 0) \rangle, \\ C_T(\mathbf{q}, t) &= \frac{1}{N} \langle \mathbf{j}_T(\mathbf{q}, t) \cdot \mathbf{j}_T(-\mathbf{q}, 0) \rangle, \end{aligned} \quad (1)$$

where $\mathbf{j}_L(\mathbf{q}, t)$ and $\mathbf{j}_T(\mathbf{q}, t)$ are given by

$$\begin{aligned}\mathbf{j}_L(\mathbf{q}, t) &= \sum_i^N (\mathbf{v}_i(t) \cdot \hat{\mathbf{q}}) \hat{\mathbf{q}} e^{i\mathbf{q} \cdot \mathbf{r}_i(t)}, \\ \mathbf{j}_T(\mathbf{q}, t) &= \sum_i^N [\mathbf{v}_i(t) - (\mathbf{v}_i(t) \cdot \hat{\mathbf{q}}) \hat{\mathbf{q}}] e^{i\mathbf{q} \cdot \mathbf{r}_i(t)},\end{aligned}\quad (2)$$

with N , \mathbf{q} , \mathbf{r}_i , and \mathbf{v}_i representing the total number of atoms, wave vector, atomic position vector, and velocity vector, respectively. For comparison, Fig. 2d also shows the renormalized phonon dispersions at 25 K and 250 K using gray lines, calculated using the temperature-dependent effective potential (TDEP) [45] based on the $P\bar{3}m1$ structure. TDEP incorporates temperature-dependent phonon frequency correction arising from lattice anharmonicity beyond the third order. At 250 K, the phonon modes are well-defined and all real, with frequencies from current correlation functions closely matching those derived from TDEP calculations, which reveals that higher-than-third-order anharmonic renormalization to harmonic phonon frequencies (see Fig. S18) at 0 K. In contrast, phonon scattering at 25 K is significantly more severe than at 250 K, especially along the wave vector paths from Γ to A and from M to Γ in the first BZ, indicating substantial phonon-disorder interactions. Additionally, we observe unusual overdamped modes near the BZ center at 25 K, as similarly observed in perovskite CsPbBr_3 at 385 K in the tetragonal phase and 500 K in the cubic phase [46], while no imaginary modes are observed in TDEP results. This comparison suggests that lattice dynamics based on ordered crystalline $\text{Cs}_3\text{Bi}_2\text{I}_6\text{Cl}_3$ is not suitable for comprehending vibrational modes and heat transport of $\text{Cs}_3\text{Bi}_2\text{I}_6\text{Cl}_3$ at low temperatures.

To rationalize the large lattice distortion, we computed potential energy surfaces (PES) of the imaginary phonon modes at high-symmetry points by displacing corresponding atoms along their eigenvectors. We found shallow and double-well PES shown in Fig. 2e (for Γ point) and Fig. S18 (for other high-symmetry points), leading to significant atomic displacements towards two local minima with large distances of about 0.7 Å. In Fig. 2e, the energy barrier along the imaginary mode of Γ point is only 0.7 meV/atom, which is about the energy scale of thermal fluctuations at about 10 K. The shallow double-well PES associated with imaginary modes from the low-frequency branch along the Γ -A-M- Γ -K path (Fig. S18) collectively drive lattice distortion in $\text{Cs}_3\text{Bi}_2\text{I}_6\text{Cl}_3$. This branch collapse typically correlates with overall structural disorder, rather than an isolated soft mode driving a phase transition to an ordered phase with lower symmetry. After the distortion, the atoms in the distorted structure exhibit local vibrations with negligible MSD (see Fig. S8) around their new equilibrium positions, without any observable hopping behavior. The calculated harmonic vibrational density of states (see Fig. S9) for these distorted structures further confirms the absence of imaginary frequencies.

Lattice distortions in crystals are often attributed to atomic

size mismatch [47], i.e.

$$\delta\% = 100\% \sqrt{\sum_{i=1}^n c_i \left(1 - \frac{r_i}{\sum_{j=1}^n c_j r_j}\right)^2}, \quad (3)$$

where c_i and r_i denote the atomic fraction and atomic radius of the i th element, respectively. High-entropy alloys (HEAs) with large δ often have strong lattice distortions [48]. In comparison, the δ of $\text{Cs}_3\text{Bi}_2\text{I}_6\text{Cl}_3$ is larger than that of typical HEAs, as shown in Fig. 2f. The δ mainly come from the large difference in atomic radii of Cs and Cl. The large δ not only shed light on the large lattice distortions, but also help explain why the κ of $\text{Cs}_3\text{Bi}_2\text{I}_9$ exhibits typical crystalline behavior [49] while the κ of $\text{Cs}_3\text{Bi}_2\text{I}_6\text{Cl}_3$ is glassy.

Thermal conductivity follows a glass-like mechanism

We computed the κ of $\text{Cs}_3\text{Bi}_2\text{I}_6\text{Cl}_3$ using both molecular dynamics and lattice dynamics. Classical MD simulations with Green-Kubo (GK) theory offer a straightforward method to compute the κ of disordered crystals, as atomic disorder is inherently included. At T above 150 K, the computed κ (see Fig. S15) agree well with our experimental data. However, below 150 K, the calculations show a distinct overestimation, due to the lack of NQEs in classical MD. To include NQEs, we also performed TRPMD simulations with GK theory. The κ calculated from TRPMD (see Fig. S15) does not show considerable differences from those computed using classical MD (i.e., still overestimating the experimental κ at T below 150 K), indicating potential limitations of the GK method within TRPMD for accurately assessing κ at low T . One possible limitation arises from the ambiguous definition of the non-linear heat flux operator in PIMD-based simulations [22, 23]. In addition, any PIMD- or RPMD-based techniques are designed to sample quantum-mechanical distributions and cannot unambiguously capture real-time dynamics, limiting their ability to accurately compute heat flux. We stress that the origin of the discrepancy between GK thermal conductivity predictions from classical or PIMD-based simulations and experimental results at extremely low temperatures remains unclear and warrants further investigations.

Classical homogeneous non-equilibrium MD (HNEMD) simulations [50, 51], with an empirical quantum correction [52] (detailed in Methods), provide an alternative way to assess κ without defining the heat flux in the PIMD-based framework. The κ from HNEMD are shown in Fig. 3. Our classical and quantum-corrected HNEMD results show good agreement with the experimental data above 150 K. Classical HNEMD κ show an overestimation along both the x and z directions at T below 150 K compared to the measurements, similar to the observation from the GK results with classical MD. After applying the harmonic quantum correction [52] accounting for the modal heat capacity, the corrected κ_z agrees well with the experimental data. However, κ_x remains overestimated and fails to reproduce the glassy behavior. This may be due to the limited scope of the harmonic quantum correction, which considers only the empirical correction of quantum

effects on the heat capacity, but does not address mode-mode occupations that can affect phonon coupling.

As the MD based methods are not able to reproduce the experimental glassy κ of $\text{Cs}_3\text{Bi}_2\text{I}_6\text{Cl}_3$, we resorted to lattice dynamics, which can incorporate the Bose-Einstein statistics of atomic vibration, also structure disorder [33] and anharmonicity [26]. For disordered $\text{Cs}_3\text{Bi}_2\text{I}_6\text{Cl}_3$ below 200 K, the lack of periodicity results in a thermodynamically large primitive cell, restricting WTE to contribute κ from $\mathbf{q} = \mathbf{0}$. Therefore, we employed the WTE [25] at $\mathbf{q} = \mathbf{0}$ to compute the κ of disordered $\text{Cs}_3\text{Bi}_2\text{I}_6\text{Cl}_3$ below 200 K:

$$\kappa = \frac{1}{\mathcal{V}N_c} \sum_{\mathbf{q},s,s'} \frac{\omega(\mathbf{q})_s + \omega(\mathbf{q})_{s'}}{4} \left(\frac{C(\mathbf{q})_s}{\omega(\mathbf{q})_s} + \frac{C(\mathbf{q})_{s'}}{\omega(\mathbf{q})_{s'}} \right) \frac{\|\mathbf{v}(\mathbf{q})_{s,s'}\|^2}{3} \times \pi \mathcal{F}_{[\Gamma(\mathbf{q})_s + \Gamma(\mathbf{q})_{s'}]}(\omega(\mathbf{q})_s - \omega(\mathbf{q})_{s'}), \quad (4)$$

where \mathcal{V} is the volume of the unit cell, N_c is the number of \mathbf{q} -points in the summation, s and s' are band indices at the wave vector \mathbf{q} (with κ_P derived when $s = s'$ and κ_C derived when $s \neq s'$), ω is the vibrational frequency, $C(\mathbf{q})_s$ is the specific heat, and $\mathbf{v}(\mathbf{q})_{s,s'}$ is the velocity operator. $\Gamma(\mathbf{q})_s$ is the anharmonic linewidth, and the Lorentzian distribution \mathcal{F} , having a full width at half maximum (FWHM) equal to $\Gamma(\mathbf{q})_s + \Gamma(\mathbf{q})_{s'}$, is defined as:

$$\mathcal{F}_{[\Gamma(\mathbf{q})_s + \Gamma(\mathbf{q})_{s'}]}(\omega(\mathbf{q})_s - \omega(\mathbf{q})_{s'}) = \frac{1}{\pi} \frac{\frac{1}{2} (\Gamma(\mathbf{q})_s + \Gamma(\mathbf{q})_{s'})}{(\omega(\mathbf{q})_s - \omega(\mathbf{q})_{s'})^2 + \frac{1}{4} (\Gamma(\mathbf{q})_s + \Gamma(\mathbf{q})_{s'})^2}. \quad (5)$$

Ideally, an infinitely large supercell is required to fully capture lattice disorder. Practically, we approximated this by using relaxed distorted supercells of 252, 896, 1750, 3024 and 4116 atoms to compute WTE κ at $\mathbf{q} = \mathbf{0}$. The relaxed structures, classified as $P1$ symmetry (see Fig. 3), were used as the initial equilibrium configuration to compute group velocities and frequencies (see Methods for details). Given the computational expense of calculating anharmonic linewidths for large unit cells, we employed the widely used approximation that determines the linewidths as a function of frequency (see Methods, as well as Fig. S19 and Tabel S3 of SI).

The WTE thermal conductivities exhibit variations with supercell size (Fig. S11), reflecting the combined influence of finite-size effects and atomic disorder. Increasing the simulation cell's size yields a reduction of finite-size effects. Notably, the thermal conductivities computed for 3024-atom and 4116-atom supercells show relatively small differences. In Fig. 3, we present the WTE results using the 4116-atom supercell. We observe that WTE thermal conductivities along both the x and z directions decrease with temperature below 50 K, contrasting with classical HNEMD and GK results but aligning more closely with experimental observations. Furthermore, from 25 K to 200 K, WTE results agree well with experiments within the uncertainty range. This comparison suggests that WTE, applied to distorted structures, effectively reproduces the glass-like thermal conductivities observed experimentally, particularly at extremely low temperatures.

We emphasize that the glass-like κ of $\text{Cs}_3\text{Bi}_2\text{I}_6\text{Cl}_3$ below 200 K is mainly determined by structural disorder. This conclusion is further supported by an anharmonicity sensitivity analysis (see Fig. S20), which shows that artificially doubling or halving the intrinsic linewidths yields unimportant changes in both κ_x and κ_z . This behavior is fundamentally different from that observed in simple crystals having κ limited by anharmonicity [53], where doubling (halving) the linewidth directly halves (doubles) the conductivity. These findings confirm that in $\text{Cs}_3\text{Bi}_2\text{I}_6\text{Cl}_3$ below 200 K, structural disorder dominates over anharmonicity in limiting heat conduction, resulting in a conductivity displaying the glass-like temperature dependence observed in experiments.

For the ordered $P\bar{3}m1$ phase at high T (250 K and 300 K), the WTE predicts the bulk limit of κ by integrating phonon properties over the entire BZ of the crystal [25]. We used this structure in the WTE calculation, which accounts for thermal expansion, renormalized phonon frequencies using TDEP [45], and four-phonon interactions [54, 55], essential corrections to accurately treat perovskites with strong lattice anharmonicity [56]. The calculated values of κ are consistent with the experimental observations as shown in Fig. 3. Further insights into thermal transport are obtained from the spectral- κ at 300 K, as shown in Fig. S16. Notably, κ_P exhibits an extremely low value of ~ 0.18 W/mK at 300 K along both x and z directions, and κ_C along the z -axis is almost equal to κ_P along the z -axis, implying considerable wavelike-tunneling heat transport in $\text{Cs}_3\text{Bi}_2\text{I}_6\text{Cl}_3$ at room temperature. Note that the experimental κ above 200 K exhibits a subtle increase with temperature, which apparently deviates from the conventional T^{-1} trend. This slight increase of κ in crystalline $\text{Cs}_3\text{Bi}_2\text{I}_6\text{Cl}_3$ above 200 K can be attributed to the contribution from the coherence transport channel, which contribute to an additional wave-like κ_C , as observed in complex crystals such as Ag_8GeSe_6 [57].

Finally, we rule out two other possible factors that may affect the κ comparisons between calculations and measurements. To examine phonon-boundary scattering effects, we computed the spectral mean free path (MFP) of $\text{Cs}_3\text{Bi}_2\text{I}_6\text{Cl}_3$ at 25 K. At 25 K, the maximum MFP (Fig. S17) along the x direction is approximately 400 nm, which is significantly shorter than the dimensions of the single crystal sample ($2.5 \times 2.5 \times 6$ mm³) used to measure κ . We also examined the phonon-isotope effects [58] by considering different isotope masses in HNEMD simulations, and find that these effects are negligible for κ .

In summary, we synthesized a single-crystal inorganic halide perovskite $\text{Cs}_3\text{Bi}_2\text{I}_6\text{Cl}_3$ and measure its glassy κ from 20 K to 300 K. We developed a machine-learning neuroevolution potential and performed PIMD simulations to investigate its atomic structure. The atomic probability distribution from PIMD trajectories reveal an disorder-to-order transition at ~ 200 K, indicating significant lattice distortion in $\text{Cs}_3\text{Bi}_2\text{I}_6\text{Cl}_3$. Given the disordered structure in $\text{Cs}_3\text{Bi}_2\text{I}_6\text{Cl}_3$ at low temperatures, we employed both lattice dynamics and molecular dynamics approaches to compute its κ . We concluded that evaluating the glass limit of the WTE in our structurally distorted atomistic models of $\text{Cs}_3\text{Bi}_2\text{I}_6\text{Cl}_3$ (i.e., a calculation at

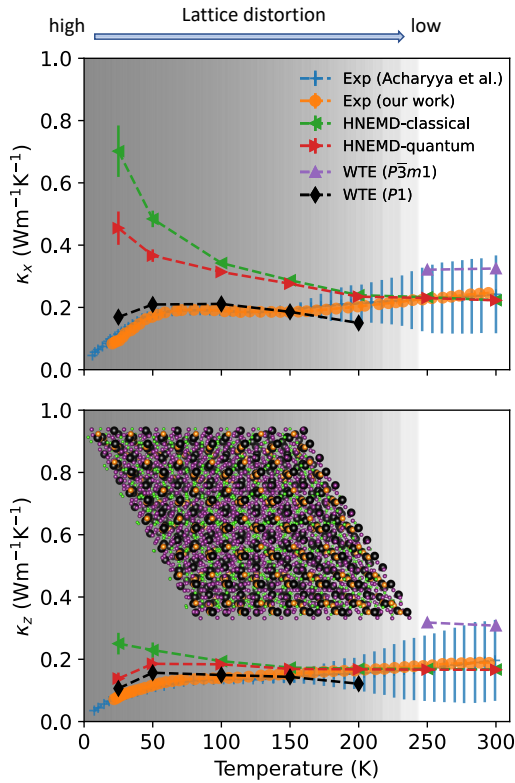


FIG. 3. Calculated κ for single crystal $\text{Cs}_3\text{Bi}_2\text{I}_6\text{Cl}_3$. Green and red triangles show results from homogeneous nonequilibrium MD (HNEMD) simulations, with and without empirical quantum corrections. At 250 K and 300 K, the purple triangles show the κ calculated using the Wigner Transport Equation (WTE) with $P\bar{3}m1$ structure with Fourier interpolation. At T between 25 K and 200 K, the diamonds show the WTE κ on top of the relaxed distorted structures (4116 atoms) computed at only Γ point (center of the Brillouin zone). A relaxed disordered structure at 25 K is shown in the inset. Additionally, the circle and cross symbols show experimental κ from our measurements and from Ref. [10], respectively.

$\mathbf{q} = \mathbf{0}$ only in a model containing more than four thousands atoms) rationalizes the glassy κ below 200 K. Moreover, the nearly temperature-independent conductivity of the ordered crystal $\text{Cs}_3\text{Bi}_2\text{I}_6\text{Cl}_3$ at and above 250 K originates from strong wave-like tunneling transport, as explained by the solution of the WTE in the complex crystal regime (i.e., a calculation involving an integration of phonon properties over the entire BZ). Our κ computation workflow considers both nuclear quantum effects and atomic disorder, providing a framework for comprehending and modeling heat transport in disordered materials.

METHODS

Experiments

Sample preparation The raw materials CsCl (99.9%, Innochem) and BiI_3 (99.99%, Aladdin) were sealed in a quartz tube and placed in a two-zone vertical furnace. The tube was gradually heated to 1023 K, where it was maintained for 40 hours. Subsequently, the lower zone of the furnace was cooled to 903 K over an 8-hour period. The temperatures in both zones were then decreased at a rate of 3 K/h for a total of 90 hours. Finally, the heating was turned off to complete the cooling process, allowing the resulting $\text{Cs}_3\text{Bi}_2\text{I}_6\text{Cl}_3$ to crystallize.

Sample characterization Single-crystal X-ray diffraction (XRD) studies were performed on a Bruker D8 QUEST diffractometer equipped with a $\text{Mo K}\alpha$ radiation source ($\lambda = 0.71073 \text{ \AA}$) at room temperature. The crystal structure solution and refinements of $\text{Cs}_3\text{Bi}_2\text{I}_6\text{Cl}_3$ is carried out using single crystal XRD at room temperature, as shown in Table S2. The $\text{Cs}_3\text{Bi}_2\text{I}_6\text{Cl}_3$ sample possesses the trigonal structure with a space group $P\bar{3}m1$. As presented in Figure S1, all the peaks of powder XRD pattern fit well with the $\text{Cs}_3\text{Bi}_2\text{I}_6\text{Cl}_3$ pattern. The XRD pattern tested on the cleavage plane shows that the crystal is liable to fracture along the $(00l)$ crystal plane due to the weak chemical bonds between the layers.

Thermal conductivity measurement The cleavage plane of crystalline $\text{Cs}_3\text{Bi}_2\text{I}_6\text{Cl}_3$ is the $(00l)$ (l is an integer) plane. To measure the κ in the cleavage plane (κ_x or κ_y) and across the cleavage plane (κ_z), two cubes (sectional area: $2.5 \text{ mm} \times 2.5 \text{ mm}$; height: 6 mm) were cut from the obtained crystal for the thermal conductivity measurement. The low-temperature κ was measured using a physical properties measurement system (PPMS, Quantum Design). The $\text{Cs}_3\text{Bi}_2\text{I}_6\text{Cl}_3$ crystal is nonconductive [10], so the measured thermal conductivity is equal to the lattice thermal conductivity. Our measurements of κ agree very well with the previous experiments [10].

Calculations

Constructing the MLP. We utilized the neural-network-based neuroevolution potential (NEP) approach [36] to develop a MLP for $\text{Cs}_3\text{Bi}_2\text{I}_6\text{Cl}_3$. The procedure begins with obtaining the relaxed structure at 0 K using the VASP package [59, 60]. Subsequently, we conducted *ab initio* molecular dynamics (AIMD) simulations in the NVT ensemble with a $2 \times 2 \times 2$ supercell (112 atoms) at temperatures of 20 K, 50 K, 100 K, 200 K, 300 K, 400 K, 500 K, and 600 K, randomly selecting ~ 50 configurations for training at each temperature. Furthermore, AIMD simulations with the NPT ensemble, varying pressure ($\pm 1 \text{ Gpa}$ and 2.5 Gpa) at specific temperatures (25 K, 150 K and 300 K), were performed and ~ 30 configurations were randomly chosen for each condition to account for lattice thermal expansion. Taking into account the two-dimensional layered structure of $\text{Cs}_3\text{Bi}_2\text{I}_6\text{Cl}_3$, we further selected configurations using the initial NEP, conducting MD simulations with D3 dispersion correction [61] at 25 K, 100 K, 200 K, and 300 K. The final training set comprises 1000 configurations.

We used the PBEsol functional [38] in the DFT calculations, known for its accuracy in predicting lattice constants and κ in strongly anharmonic crystals [62]. All AIMD simulations employ an energy cutoff value of 400 eV and a Γ -centered $1 \times 1 \times 1$ k -point mesh with the PBEsol [38] functional. We raised the energy cutoff to 550 eV with a denser $3 \times 3 \times 3$ k -point mesh to perform accurate single-point DFT calculations and obtain the energies and atomic forces of the selected configurations. We used the GPUMD package [63] to train the NEP model, and the final training/test root mean square errors (RMSEs) for energy, atomic force, and virial are 0.35/0.33 meV/atom, 0.027/0.026 eV/Å, and 3.79/3.33 meV/atom, respectively.

Cross validation of the NEP model. To validate our NEP model, we performed path integral molecular dynamics (PIMD) simulations at selected temperatures (25 K, 100 K, 300 K, and 400 K), both with and without the D3 correction, and sampled a number of configurations for subsequent single-point DFT calculations. Parity plots between NEP and DFT for the energies and forces of the sampled configurations are presented in Figs. S2 and S3. Without the D3 correction, The RMSEs for energy and force are 0.36 meV/atom and 0.025 eV/Å, respectively, while they are 0.31 meV/atom and 0.021 eV/Å, respectively, with the D3 correction. The lattice constants (Table S1) and atomic potential energy surfaces of some soft modes (Fig. S12) from DFT and NEP calculations are in good agreement.

MD simulations We performed MD simulations using the GPUMD package [63], for which PIMD techniques have been implemented recently [64]. The integration time step was set to 1 fs in both classical and PIMD related simulations. PIMD/RPMD simulations were conducted at 25 K and 50 K with 64 beads, at 100 K, 150 K, and 200 K with 32 beads, and at 250 K and 300 K with 16 beads. Convergence tests for the number of beads in these simulations are provided in Fig. S14. For quantum MD simulations, we started with PIMD simulations in an NPT ensemble to obtain equilibrium structures at the specified temperatures. Following this, we run 0.5 ns RPMD simulations to collect atomic trajectories to calculate atomic probability distributions and radial distribution functions, or TRPMD simulations to compute κ based on the Green-Kubo relationship. Further details on the computation of κ using Green-Kubo theory with TRPMD simulations are available in Fig. S9 and Note S1 of SI. For classical HNEMD simulations, we used an NPT ensemble, employing a stochastic cell rescaling barostat [65] in combination with the stochastic velocity rescaling thermostat [66] to calculate κ . We conducted a thorough examination of size effects and the selection of external forces during HNEMD simulations.

Anharmonic linewidths and its analytical function Calculating vibrational linewidths rigorously in a complex, atom-heavy primitive cell is highly time-consuming. To address this challenge, previous studies [31, 33, 67] introduced a coarse-grained function, $\Gamma_a[\omega]$, in various formats to reduce computational demands. The only required input to obtain $\Gamma_a[\omega]$ is the exact linewidths at $\mathbf{q} = 0$. Simoncelli *et al.* [31] demonstrated that the use of the single-valued function $\Gamma_a[\omega]$ leads to practically identical results for the conductivity of rWTE compared to exact linewidths. This fitting was demonstrated

to reliably capture the linewidths of ν -SiO₂ [31], Mg₂Si_{1-x}Sn_x [67], amorphous Si [32] and Al₂O₃ [33].

Here we used the RPMD simulations with normal mode decomposition method [68, 69] to obtain the exact anharmonic linewidths of all vibrational modes at $\mathbf{q} = 0$, and then we fit [31] the $\Gamma_a[\omega]$ as

$$\Gamma_a[\omega] = \frac{1}{\sqrt{\frac{1}{(\Gamma_1[\omega])^2} + \frac{1}{(\Gamma_2[\omega])^2}}}, \quad (6)$$

where $\Gamma_1[\omega]$ and $\Gamma_2[\omega]$ are defined as

$$\Gamma_1[\omega] = \frac{\sum_{\mathbf{q}=0,s} \frac{1}{\sqrt{2\pi\sigma^2}} \exp\left[-\frac{\hbar^2(\omega(\mathbf{q})_s - \omega)^2}{2\sigma^2}\right]}{\sum_{\mathbf{q}=0,s} \frac{1}{\Gamma(\mathbf{q})_s \sqrt{2\pi\sigma^2}} \exp\left[-\frac{\hbar^2(\omega(\mathbf{q})_s - \omega)^2}{2\sigma^2}\right]}, \quad (7)$$

$$\Gamma_2[\omega] = p \cdot \omega^2, \\ p = \frac{\sum_{\mathbf{q}=0,s} \int_{\omega_0}^{2\omega_0} d\omega_c \frac{\Gamma(\mathbf{q})_s}{\omega^2(\mathbf{q})_s \sqrt{2\pi\sigma^2}} \exp\left[-\frac{\hbar^2(\omega(\mathbf{q})_s - \omega_c)^2}{2\sigma^2}\right]}{\sum_{\mathbf{q}=0,s} \int_{\omega_0}^{2\omega_0} d\omega_c \frac{1}{\sqrt{2\pi\sigma^2}} \exp\left[-\frac{\hbar^2(\omega(\mathbf{q})_s - \omega_c)^2}{2\sigma^2}\right]}. \quad (8)$$

Here, ω_0 is the smallest non-zero frequency when $\mathbf{q} = 0$, and $\sigma = 70 \text{ cm}^{-1}$ is a broadening parameter set large enough to ensure smooth averaging of linewidths. The full-order lattice anharmonicity is intrinsically considered for anharmonic linewidths extracted from the normal mode decomposition with ring-polymer or classical MD simulations (see Fig. S5 of SI for comparisons).

WTE thermal conductivity of disordered Cs₃Bi₂I₆Cl₃ At low temperatures (25 K to 200 K), RPMD simulations were performed for supercells of different sizes with $\bar{P}3m1$ structure at various temperatures. A configuration randomly extracted from the equilibrium stage was then relaxed, and the resulting structures were used as the initial distorted configurations. Harmonic force constants were computed using the finite displacement method implemented in the Phonopy package [70–72]. Frequencies and group velocity matrices for vibrational modes at $\mathbf{q} = \mathbf{0}$ were derived from the harmonic force constants using the Phono3py package [70–72]. The physical linewidths were obtained from normal mode decomposition with RPMD trajectories, and analytical linewidths were fitted as described above. Figure S12 provides a detailed workflow for computing WTE κ at $\mathbf{q} = \mathbf{0}$ for disordered materials.

WTE thermal conductivity of crystal Cs₃Bi₂I₆Cl₃ We obtained the temperature-dependent cubic and quartic interatomic force constants (IFCs) at 250 K and 300 K using the hiPhive package [73]. The harmonic terms at 0 K calculated using Phonopy [70] were subtracted from the atomic forces and only cubic and quartic IFCs were extracted to the residual force-displacement data. We collected the force-displacement data from RPMD simulations. Three-phonon linewidths were calculated using the ShengBTE [74] package. Four-phonon linewidths were calculated using our code based on the formulae developed by Feng *et al.* [54, 55]. We carefully tested

the relation between q -point mesh and κ , and a $6 \times 6 \times 6$ q -point mesh was used to compute the phonon linewidths and the κ of $\text{Cs}_3\text{Bi}_2\text{I}_6\text{Cl}_3$. The scalebroad parameter for Gaussian smearing used for numerically ensuring the energy conservation process in phonon-phonon scatterings was set to 1 and 0.1 for the calculations of the three- and four-phonon scatterings, respectively. We also calculated the WTE conductivity based on our experimental lattice constants at 300 K, and the calculated WTE κ ($\kappa_x = 0.227 \text{ Wm}^{-1}\text{K}^{-1}$; $\kappa_z = 0.231 \text{ Wm}^{-1}\text{K}^{-1}$) based on experimental lattice constants show a better agreement with the measurements, compared to those based on the predicted lattice constants of NEP.

HNEMD and its quantum correction In HNEMD [50, 51], one applies an external driving force

$$\mathbf{F}_i^{\text{ext}} = \mathbf{F}_e \cdot \mathbf{W}_i \quad (9)$$

to generate a nonzero heat current. Here \mathbf{F}_e is the driving force parameter and \mathbf{W}_i is the virial tensor for atom i . Within the linear-response regime, the heat current \mathbf{J} is proportional to the driving force parameter as

$$\langle \mathbf{J}^\alpha \rangle = TV \sum_{\beta} \kappa^{\alpha\beta} \mathbf{F}_e^\beta, \quad (10)$$

where V is the volume of the simulated system, and α and β are Cartesian directions. Considering diagonal elements of the thermal conductivity tensor and dropping the tensor indices, the cumulative thermal conductivity in one direction can be expressed as

$$\kappa(t) = \frac{1}{t} \int_0^t ds \frac{\langle \mathbf{J}(s) \rangle}{TV\mathbf{F}_e}. \quad (11)$$

The HNEMD approach [50] also allows for obtaining the spectral thermal conductivity

$$\kappa(\omega, T) = \frac{2}{VTF_e} \int_{-\infty}^{\infty} dt e^{i\omega t} K(t), \quad (12)$$

Here, $K(t)$ is the virial-velocity correlation function and its vectorial version is defined as

$$\mathbf{K}(t) = \sum_i \langle \mathbf{W}_i(0) \cdot \mathbf{v}_i(t) \rangle. \quad (13)$$

The classical spectral thermal conductivity $\kappa(\omega, T)$ can be quantum-corrected [52, 75] by multiplying it with the ratio of quantum-to-classical modal heat capacity:

$$\kappa^q(\omega, T) = \kappa(\omega, T) \frac{x^2 e^x}{(e^x - 1)^2}, \quad (14)$$

where $x = \hbar\omega/(k_B T)$.

Spectral Mean free path To compute the vibrational mean free paths (MFPs) of the vibrational modes, we first perform a single NEMD simulation in the ballistic limit (low T and short supercell length L), equivalent to the atomistic Green's function approach, and then employ the same spectral decomposition method as in HNEMD to obtain the spectral thermal conductance $G(\omega)$ [52]:

$$G(\omega) = \frac{2}{V\Delta T} \int_{-\infty}^{\infty} dt e^{i\omega t} K(t), \quad (15)$$

where ΔT is the temperature difference between the heat source and the heat sink in the NEMD setup. Then we can derive the spectral MFP as [50]

$$\lambda(\omega, T) = \kappa(\omega, T)/G(\omega). \quad (16)$$

Acknowledgments ZZ acknowledges the European Union's Horizon 2020 research and innovation programme under the Marie Skłodowska-Curie grant agreement No 101034413. The authors acknowledge the research computing facilities offered by HPC ISTA and ITS HKU.

-
- [1] R. Peierls, "Zur kinetischen theorie der wärmeleitung in kristallen," *Annalen der Physik* **395**, 1055 (1929).
- [2] Z. Zeng, X. Shen, R. Cheng, O. Perez, N. Ouyang, Z. Fan, P. Lemoine, B. Raveau, E. Guilmeau, and Y. Chen, "Pushing thermal conductivity to its lower limit in crystals with simple structures," *Nature Communications* **15**, 3007 (2024).
- [3] W. Lee, H. Li, A. B. Wong, D. Zhang, M. Lai, Y. Yu, Q. Kong, E. Lin, J. J. Urban, J. C. Grossman, *et al.*, "Ultralow thermal conductivity in all-inorganic halide perovskites," *Proceedings of the National Academy of Sciences* **114**, 8693 (2017).
- [4] D. G. Cahill, "Thermal conductivity measurement from 30 to 750 K: the 3ω method," *Review of Scientific Instruments* **61**, 802 (1990).
- [5] J. J. Freeman and A. C. Anderson, "Thermal conductivity of amorphous solids," *Physical Review B* **34**, 5684 (1986).
- [6] P. W. Anderson, B. I. Halperin, and C. M. Varma, "Anomalous low-temperature thermal properties of glasses and spin glasses," *Philosophical Magazine* **25**, 1 (1972).
- [7] W. Schirmacher, G. Ruocco, and T. Scopigno, "Acoustic attenuation in glasses and its relation with the boson peak," *Physical Review Letters* **98**, 025501 (2007).
- [8] P. B. Allen and J. L. Feldman, "Thermal conductivity of glasses: Theory and application to amorphous Si," *Physical Review Letters* **62**, 645 (1989).
- [9] P. B. Allen and J. L. Feldman, "Thermal conductivity of disordered harmonic solids," *Physical Review B* **48**, 12581 (1993).
- [10] P. Acharyya, T. Ghosh, K. Pal, K. S. Rana, M. Dutta, D. Swain, M. Etter, A. Soni, U. V. Waghmare, and K. Biswas, "Glassy thermal conductivity in $\text{Cs}_3\text{Bi}_2\text{I}_6\text{Cl}_3$ single crystal," *Nature Communications* **13**, 5053 (2022).
- [11] B. Sun, S. Niu, R. P. Hermann, J. Moon, N. Shulumba, K. Page, B. Zhao, A. S. Thind, K. Mahalingam, J. Milam-Guerrero, *et al.*, "High frequency atomic tunneling yields ultralow and glass-like thermal conductivity in chalcogenide single crystals," *Nature Communications* **11**, 6039 (2020).
- [12] B. Zhao, M. S. B. Hoque, G. Y. Jung, H. Mei, S. Singh, G. Ren,

- M. Milich, Q. Zhao, N. Wang, H. Chen, *et al.*, “Orientation-controlled anisotropy in single crystals of quasi-1D BaTiS₃,” *Chemistry of Materials* **34**, 5680 (2022).
- [13] M. S. B. Hoque, E. R. Hoglund, B. Zhao, D.-L. Bao, H. Zhou, S. Thakur, E. Osei-Agyemang, K. Hattar, E. A. Scott, M. Surendran, *et al.*, “Ruddlesden-popper chalcogenides push the limit of mechanical stiffness and glass-like thermal conductivity in crystals,” arXiv preprint arXiv:2312.02534 (2023).
- [14] D. G. Cahill, S. K. Watson, and R. O. Pohl, “Lower limit to the thermal conductivity of disordered crystals,” *Physical Review B* **46**, 6131 (1992).
- [15] M. Beekman and D. G. Cahill, “Inorganic crystals with glass-like and ultralow thermal conductivities,” *Crystal Research and Technology* **52**, 1700114 (2017).
- [16] B. C. Sales, B. Chakoumakos, R. Jin, J. Thompson, and D. Mandrus, “Structural, magnetic, thermal, and transport properties of X₈Gal₆Ge₃₀ (X = Eu, Sr, Ba) single crystals,” *Physical Review B* **63**, 245113 (2001).
- [17] B. Zink, R. Pietri, and F. Hellman, “Thermal conductivity and specific heat of thin-film amorphous silicon,” *Physical Review Letters* **96**, 055902 (2006).
- [18] M. Parrinello and A. Rahman, “Study of an F center in molten KCl,” *The Journal of Chemical Physics* **80**, 860 (1984).
- [19] J. Cao and G. A. Voth, “The formulation of quantum statistical mechanics based on the feynman path centroid density. iv. algorithms for centroid molecular dynamics,” *The Journal of Chemical Physics* **101**, 6168 (1994).
- [20] S. Habershon, D. E. Manolopoulos, T. E. Markland, and T. F. Miller III, “Ring-polymer molecular dynamics: Quantum effects in chemical dynamics from classical trajectories in an extended phase space,” *Annual Review of Physical Chemistry* **64**, 387 (2013).
- [21] M. Rossi, M. Ceriotti, and D. E. Manolopoulos, “How to remove the spurious resonances from ring polymer molecular dynamics,” *The Journal of Chemical Physics* **140** (2014).
- [22] R. Luo and K. Yu, “Capturing the nuclear quantum effects in molecular dynamics for lattice thermal conductivity calculations: Using ice as example,” *The Journal of Chemical Physics* **153** (2020).
- [23] B. J. Sutherland, W. H. Moore, and D. E. Manolopoulos, “Nuclear quantum effects in thermal conductivity from centroid molecular dynamics,” *The Journal of Chemical Physics* **154** (2021).
- [24] G. Caldarelli, M. Simoncelli, N. Marzari, F. Mauri, and L. Benfatto, “Many-body green’s function approach to lattice thermal transport,” *Physical Review B* **106**, 024312 (2022).
- [25] M. Simoncelli, N. Marzari, and F. Mauri, “Unified theory of thermal transport in crystals and glasses,” *Nature Physics* **15**, 809 (2019).
- [26] M. Simoncelli, N. Marzari, and F. Mauri, “Wigner formulation of thermal transport in solids,” *Physical Review X* **12**, 041011 (2022).
- [27] L. Isaeva, G. Barbalinardo, D. Donadio, and S. Baroni, “Modeling heat transport in crystals and glasses from a unified lattice-dynamical approach,” *Nature Communications* **10**, 3853 (2019).
- [28] A. Fiorentino and S. Baroni, “From Green-Kubo to the full Boltzmann kinetic approach to heat transport in crystals and glasses,” *Physical Review B* **107**, 054311 (2023), publisher: American Physical Society.
- [29] G. Barbalinardo, Z. Chen, N. W. Lundgren, and D. Donadio, “Efficient anharmonic lattice dynamics calculations of thermal transport in crystalline and disordered solids,” *Journal of Applied Physics* **128** (2020).
- [30] J. L. Feldman, M. D. Kluge, P. B. Allen, and F. Wooten, “Thermal conductivity and localization in glasses: Numerical study of a model of amorphous silicon,” *Physical Review B* **48**, 12589 (1993).
- [31] M. Simoncelli, F. Mauri, and N. Marzari, “Thermal conductivity of glasses: first-principles theory and applications,” *npj Computational Materials* **9**, 106 (2023).
- [32] A. Fiorentino, P. Pegolo, and S. Baroni, “Hydrodynamic finite-size scaling of the thermal conductivity in glasses,” *npj Computational Materials* **9**, 157 (2023).
- [33] A. F. Harper, K. Iwanowski, W. C. Witt, M. C. Payne, and M. Simoncelli, “Vibrational and thermal properties of amorphous alumina from first principles,” *Physical Review Materials* **8**, 043601 (2024).
- [34] A recent work [53] has shown that in silica-based materials where anharmonic effects are large enough to be accurately described by the common relaxation-time approximation (like those reported here) simulations containing a few thousand atoms are sufficiently large to describe the opposite scaling laws of the conductivities of crystals and glasses upon heating. Specifically, simulations containing 6804 atoms are large enough to describe the propagation-dominated and thermally damped conductivity of AV tridymite crystal, as well as the tunneling-dominated and thermally activated conductivity of TOGA silica.
- [35] Q. He and Y. Yang, “On lattice distortion in high entropy alloys,” *Frontiers in Materials* **5**, 42 (2018).
- [36] Z. Fan, Z. Zeng, C. Zhang, Y. Wang, K. Song, H. Dong, Y. Chen, and T. Ala-Nissila, “Neuroevolution machine learning potentials: Combining high accuracy and low cost in atomistic simulations and application to heat transport,” *Physical Review B* **104**, 104309 (2021).
- [37] K. Song, R. Zhao, J. Liu, Y. Wang, E. Lindgren, Y. Wang, S. Chen, K. Xu, T. Liang, P. Ying, N. Xu, Z. Zhao, J. Shi, J. Wang, S. Lyu, Z. Zeng, S. Liang, H. Dong, L. Sun, Y. Chen, Z. Zhang, W. Guo, P. Qian, J. Sun, P. Erhart, T. Ala-Nissila, Y. Su, and Z. Fan, “General-purpose machine-learned potential for 16 elemental metals and their alloys,” *Nature Communications* **15**, 10208 (2024).
- [38] J. P. Perdew, A. Ruzsinszky, G. I. Csonka, O. A. Vydrov, G. E. Scuseria, L. A. Constantin, X. Zhou, and K. Burke, “Restoring the density-gradient expansion for exchange in solids and surfaces,” *Physical Review Letters* **100**, 136406 (2008).
- [39] S. Grimme, S. Ehrlich, and L. Goerigk, “Effect of the damping function in dispersion corrected density functional theory,” *Journal of Computational Chemistry* **32**, 1456 (2011).
- [40] D. A. Keen and A. L. Goodwin, “The crystallography of correlated disorder,” *Nature* **521**, 303 (2015).
- [41] X. Liang, J. Klarbring, W. J. Baldwin, Z. Li, G. Csányi, and A. Walsh, “Structural dynamics descriptors for metal halide perovskites,” *The Journal of Physical Chemistry C* **127**, 19141 (2023).
- [42] E. S. Božin, C. D. Malliakas, P. Souvatzis, T. Proffen, N. A. Spaldin, M. G. Kanatzidis, and S. J. Billinge, “Entropically stabilized local dipole formation in lead chalcogenides,” *Science* **330**, 1660 (2010).
- [43] E. G. Meekel and A. L. Goodwin, “Correlated disorder in metal-organic frameworks,” *CrystEngComm* **23**, 2915 (2021).
- [44] E. Fransson, M. Slabanja, P. Erhart, and G. Wahnström, “Dyna-sor—a tool for extracting dynamical structure factors and current correlation functions from molecular dynamics simulations,” *Advanced Theory and Simulations* **4**, 2000240 (2021).
- [45] O. Hellman, P. Steneteg, I. A. Abrikosov, and S. I. Simak, “Temperature dependent effective potential method for accurate free energy calculations of solids,” *Physical Review B* **87**, 104111 (2013).

- (2013).
- [46] T. Lanigan-Atkins, X. He, M. Krogstad, D. Pajeroski, D. Abernathy, G. N. Xu, Z. Xu, D.-Y. Chung, M. Kanatzidis, S. Rosenkranz, *et al.*, “Two-dimensional overdamped fluctuations of the soft perovskite lattice in CsPbBr₃,” *Nature materials* **20**, 977 (2021).
- [47] Y. Zhang, Y. J. Zhou, J. P. Lin, G. L. Chen, and P. K. Liaw, “Solid-solution phase formation rules for multi-component alloys,” *Advanced Engineering Materials* **10**, 534 (2008).
- [48] H. Song, F. Tian, Q.-M. Hu, L. Vitos, Y. Wang, J. Shen, and N. Chen, “Local lattice distortion in high-entropy alloys,” *Physical Review Materials* **1**, 023404 (2017).
- [49] P. Acharyya, K. Pal, A. Ahad, D. Sarkar, K. S. Rana, M. Dutta, A. Soni, U. V. Waghmare, and K. Biswas, “Extended antibonding states and phonon localization induce ultralow thermal conductivity in low dimensional metal halide,” *Advanced Functional Materials* **33**, 2304607 (2023).
- [50] Z. Fan, H. Dong, A. Harju, and T. Ala-Nissila, “Homogeneous nonequilibrium molecular dynamics method for heat transport and spectral decomposition with many-body potentials,” *Physical Review B* **99**, 064308 (2019).
- [51] D. J. Evans, “Homogeneous nemd algorithm for thermal conductivity—application of non-canonical linear response theory,” *Physics Letters A* **91**, 457 (1982).
- [52] Y. Wang, Z. Fan, P. Qian, M. A. Caro, and T. Ala-Nissila, “Quantum-corrected thickness-dependent thermal conductivity in amorphous silicon predicted by machine learning molecular dynamics simulations,” *Physical Review B* **107**, 054303 (2023).
- [53] M. Simoncelli, D. Fournier, M. Marangolo, E. Balan, K. Bénéut, B. Baptiste, B. Doisneau, N. Marzari, and F. Mauri, “Temperature-invariant heat conductivity from compensating crystalline and glassy transport: from the steinbach meteorite to furnace bricks,” *arXiv preprint arXiv:2405.13161* (2024).
- [54] T. Feng and X. Ruan, “Quantum mechanical prediction of four-phonon scattering rates and reduced thermal conductivity of solids,” *Physical Review B* **93**, 045202 (2016).
- [55] T. Feng, L. Lindsay, and X. Ruan, “Four-phonon scattering significantly reduces intrinsic thermal conductivity of solids,” *Physical Review B* **96**, 161201 (2017).
- [56] J. Li, L. Wei, Z. Ti, L. Ma, Y. Yan, G. Zhang, and P.-F. Liu, “Wavelike tunneling of phonons dominates glassy thermal conductivity in crystalline Cs₃Bi₂I₆Cl₃,” *Physical Review B* **108**, 224302 (2023).
- [57] T. Bernges, M. Peterlechner, G. Wilde, M. T. Agne, and W. G. Zeier, “Analytical model for two-channel phonon transport engineering,” *Materials Today Physics* **35**, 101107 (2023).
- [58] L. Lindsay, D. Broido, and T. Reinecke, “Phonon-isotope scattering and thermal conductivity in materials with a large isotope effect: A first-principles study,” *Physical Review B* **88**, 144306 (2013).
- [59] G. Kresse and J. Furthmüller, “Efficient iterative schemes for ab initio total-energy calculations using a plane-wave basis set,” *Physical Review B* **54**, 11169 (1996).
- [60] G. Kresse and D. Joubert, “From ultrasoft pseudopotentials to the projector augmented-wave method,” *Physical Review B* **59**, 1758 (1999).
- [61] P. Ying and Z. Fan, “Combining the D3 dispersion correction with the neuroevolution machine-learned potential,” *Journal of Physics: Condensed Matter* **36**, 125901 (2023).
- [62] J. Wei, Z. Xia, Y. Xia, and J. He, “Hierarchy of exchange-correlation functionals in computing lattice thermal conductivities of rocksalt and zincblende semiconductors,” *arXiv preprint arXiv:2404.06346* (2024).
- [63] Z. Fan, W. Chen, V. Vierimaa, and A. Harju, “Efficient molecular dynamics simulations with many-body potentials on graphics processing units,” *Computer Physics Communications* **218**, 10 (2017).
- [64] P. Y. et al., “Highly efficient path-integral molecular dynamics simulations with gpumd using neuroevolution potentials: Case studies on thermal properties of materials,” (2024), *arXiv:2409.04430*.
- [65] M. Bernetti and G. Bussi, “Pressure control using stochastic cell rescaling,” *The Journal of Chemical Physics* **153** (2020).
- [66] G. Bussi, D. Donadio, and M. Parrinello, “Canonical sampling through velocity rescaling,” *The Journal of Chemical Physics* **126** (2007).
- [67] S. Thebaud, T. Berlijn, and L. Lindsay, “Perturbation theory and thermal transport in mass-disordered alloys: Insights from green’s function methods,” *Physical Review B* **105**, 134202 (2022).
- [68] A. J. McGaughey and J. M. Larkin, “Predicting phonon properties from equilibrium molecular dynamics simulations,” *Annual Review of Heat Transfer* **17** (2014).
- [69] A. Carreras, A. Togo, and I. Tanaka, “Dynaphopy: A code for extracting phonon quasiparticles from molecular dynamics simulations,” *Computer Physics Communications* **221**, 221 (2017).
- [70] A. Togo and I. Tanaka, “First principles phonon calculations in materials science,” *Scripta Materialia* **108**, 1 (2015).
- [71] A. Togo, L. Chaput, T. Tadano, and I. Tanaka, “Implementation strategies in phonopy and phono3py,” *Journal of Physics: Condensed Matter* **35**, 353001 (2023).
- [72] A. Togo, “First-principles phonon calculations with phonopy and phono3py,” *Journal of the Physical Society of Japan* **92**, 012001 (2023).
- [73] F. Eriksson, E. Fransson, and P. Erhart, “The hiphive package for the extraction of high-order force constants by machine learning,” *Advanced Theory and Simulations* **2**, 1800184 (2019).
- [74] W. Li, J. Carrete, N. A. Katcho, and N. Mingo, “Shengbte: A solver of the boltzmann transport equation for phonons,” *Computer Physics Communications* **185**, 1747 (2014).
- [75] J. Turney, A. McGaughey, and C. Amon, “Assessing the applicability of quantum corrections to classical thermal conductivity predictions,” *Physical Review B* **79**, 224305 (2009).
- [76] Z. Li, Y. Xia, and C. Wolverton, “First-principles calculations of lattice thermal conductivity in Tl₃VSe₄: Uncertainties from different approaches of force constants,” *Physical Review B* **108**, 184307 (2023).